Available online at www.sciencedirect.com
SCIENCE DIRECT
ELSEVIER
European Journal of Mechanics B/Fluids 25 (2006) 471–490
EUROPEAN JOURNAL OF MECHANICS B/FLUIDS

Investigation of the impact of the geometry on the nose flow

I. Hörschler *, Ch. Brücker, W. Schröder, M. Meinke

Aerodynamisches Institut, RWTH Aachen, Wüllnerstr. zw. 5 u. 7, 52062 Aachen, Germany

Received 20 February 2005; received in revised form 24 October 2005; accepted 24 November 2005

Available online 15 February 2006

Abstract

Results for flow simulations and experiments of different models of the human nasal cavity with and without turbinates and/or spurs are presented. The flow is investigated for normal inspiration and expiration at Reynolds numbers based on the throat diameter of $Re = 500$ and $Re = 400$.

The numerical method is second-order accurate on a multi-block structured grid. Flow measurements are based on the method of Digital Particle-Image Velocimetry (DPIV) in transparent nose models. The experimental results corroborate the numerical flow structure thereby evidencing that the nose flow can be considered laminar in the Reynolds number range investigated. Moreover, the analysis of the flow field indicates overall, the higher susceptibility to geometric changes at inspiration and in particular, the lower turbinate to have the major impact on the flow structure especially when air is inhaled.

PACS: 47.11.+j; 47.15.Rq

Keywords: Nasal cavity flow; Steady and laminar flow field; Numerical and experimental investigation; Geometry variations

1. Introduction

The human nasal cavity has to satisfy a variety of different functions. Besides respiration it is responsible for moistening, tempering, and cleaning the air. These functions are expected to strongly depend on the complex internal geometry of the nasal cavity. Impaired nasal respiration especially under normal breathing conditions, i.e., in everyday life situations, is a common and widespread disease, which makes nose surgery one of the most often performed operations in the western world. Unfortunately, the success rate, i.e., the number of people having no problems after surgery, is by no means satisfactory. To enhance this situation, it is desired to numerically predict the flow field inside the nose and its relation to geometric changes. This can finally lead to a computer assisted surgery (CAS) tool [1], that will help on the one hand, to understand the flow in the extremely complex human nasal cavity and on the other hand, to derive criteria how to better predict the outcome and to improve the success of nose operations.

There are different approaches in the literature to investigate the flow field inside the nasal cavity. A recent survey on experimental and numerical findings is given, e.g., in [2]. One focus of interest is particle or odorant transport inside the nose [3]. Other intriguing issues like air-conditioning and cleaning characteristics of the nasal passage are

* Corresponding author.
E-mail address: office@aia.rwth-aachen.de (I. Hörschler).

0997-7546/$ – see front matter
doi:10.1016/j.euromechflu.2005.11.006

numerically tackled in [4,5]. A more basic numerical analysis of the flow field is presented in [6]. Those approaches investigate either only certain parts of the nasal cavity [3], they concentrate on individual patient geometries [4,7] that makes a substantial comparison almost impossible or they use abstract model geometries [6,8]. The computation in [8] is based on a two-dimensional analysis for different cross sections. In other words, no three-dimensional analysis is performed. Furthermore, the geometry possesses especially for the turbinate geometries sharp corners and edges, where shear layers evolve and the flow has to separate. That is, the flow structure around the turbinates is predefined by the simplified geometry.

In the aforementioned studies the dependence of the flow field on geometric changes is not considered due to the specialized problem definition. Geometry variations are discussed, e.g., in [9] and [10], where in the former study three geometric variations of the middle turbinate were experimentally investigated as to changes in the RMS velocity distribution and the latter analyzed the flow only qualitatively by experimentally visualizing streaklines at inspiration. Using a commercial finite volume code numerical investigations for a single individual patient geometry are discussed in [11]. The investigated Reynolds number is unknown although the flow is considered partially turbulent and a k–ϵ model is applied. The analysis lacks detailed validation with experimental results and as such no quantitative comparisons are performed to develop criteria for the prospective computer assisted surgery system. A first step to reach this long term goal of conducting some kind of virtual nose surgery is to prescribe geometric changes on a model level of the nasal cavity on the one hand, to study their effect on the overall flow field and on the other hand, to determine the parts of the nose that possess the major impact on the flow characteristics. This idea is pursued in this study. The flow fields for inspiration and expiration inside several model geometries are analyzed and compared. Furthermore, numerical and experimental findings are juxtaposed to show the validity of the numerical approach.

Note, that currently the main interest is in the major flow phenomena that can be assumed to be fairly independent of geometrical details such as hairs in the nostril or the mucous membranes inside the nasal cavity. For this reason, such geometrical intricacies are not resolved.

First, the grid generation is described, followed by a concise presentation of the numerical method of solution and the boundary conditions. Subsequently, the experimental setup is explained. Finally, the results are discussed using for instance streamline patterns, pressure and skin friction contours.

2. Numerical approach

2.1. Grid generation

For the mutual validation of the numerical and experimental findings the use of identical geometries of the nasal cavity is a must. An anatomically correct replica model with inferior and middle turbinate is constructed from the data by Masing [12,13]. The superior turbinate is neglected as it is often vestigial in average human nasal passages. In the following, we will refer to the anatomical middle as upper turbinate and the inferior will be denoted as lower turbinate.

The physical model was scanned using a computer tomograph to obtain by a marching cube algorithm applied to the CT data an unstructured surface representation. The model surface is subdivided into its main components, which are the cartilage spurs at the septum and the turbinates (Fig. 1, left). For each of these surface components two topology modules are constructed,where the first module is defined such that a grid around the component can be generated, while the second module represents a topology to create a mesh without the surface component. All topology modules of the different surface components share common boundaries. The modules can be combined arbitrarily thus giving

Table 1
Definition of several nasal cavity geometries

Case	Geometry
NC_{000}	cavity hull; no spurs, no turbinates
NC_{001}	cavity hull; no spurs, no lower turbinate
NC_{010}	cavity hull; no spurs, no upper turbinate
NC_{011}	cavity hull; no spurs, with turbinates
NC_{111}	cavity hull; with spurs and turbinates

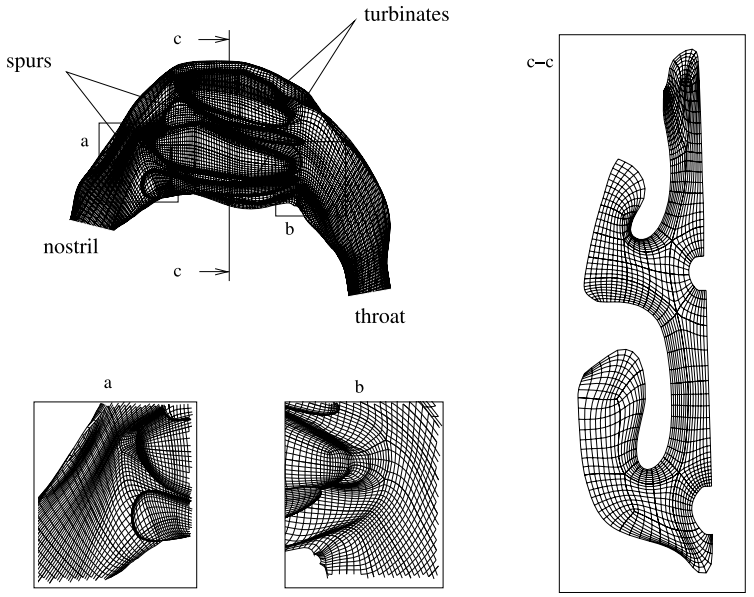

Fig. 1. Presentation of the structured multiblock grid for test case NC_{111}; (a), (b) show enlargements of the tip and tail region of the turbinates, (c) illustrates a coronal cross section.

a whole set of different structured multiblock grids for a variety of nasal cavity geometries, which can be used to analyze the influence of the surface components on the flow.

The configurations investigated in this paper are listed in Table 1 and evidenced in Fig. 2. An additional advantage of this modular grid generation is the fact that moderate geometry changes of the surface components can be locally treated in the corresponding topology module.

The grid generation is done using the commercial grid generator GridPro [14]. In Fig. 1 the grid of the NC_{111} case is shown. For each case a mesh is generated with 60,000 and 250,000 cells. Since the flow does not possess a boundary-layer-like character, no special resolution is used in the near-wall regions. The numerical calculations did converge for both resolutions down to an average residuum of 10^{-14}, which can be considered machine accuracy. Although the overall findings do coincide, i.e., the more intricate and more susceptible flow phenomena occur on the 60,000 cell and on the 250,000 cell mesh, the numerical results discussed below are based on the higher resolution since locations of vortex cores and wall shear stress distributions are better resolved on the fine mesh.

2.2. Method of solution

To simulate the flow field the dimensionless Navier–Stokes equations are solved using the flow library TFS developed at the Aerodynamisches Institut [15]. The reference values are the total density $\tilde{\rho}_0$, the speed of sound based on stagnation temperature $\tilde{a}_0$, and the diameter at the exit boundary $\widetilde{D}$, i.e., the dimensionless pressure p, velocity u, and length are $p = \tilde{p}/(\tilde{\rho}_0\tilde{a}_0^2)$, $u = \tilde{u}/\tilde{a}_0$, and $l = \tilde{l}/\widetilde{D}$. An explicit five-step Runge–Kutta method of second-order accuracy is used for temporal integration and the Runge–Kutta coefficients are optimized for a central scheme. Although the Mach number is fairly small in the flows considered, we solve the compressible equations and do not encounter any convergence problems since no purely one-sided spatial approximation is used. Following the advective upstream splitting method (AUSM) by Liou and Steffen [16] the inviscid fluxes F_α^I are split into a convective and a pressure term. The convective expression is reformulated by inserting the local sound speed c

$$F_\alpha^I = F_\alpha^c + F_\alpha^p = \frac{U_\alpha}{c}\begin{pmatrix}\rho c\\ \rho c u_\beta\\ \rho c(E + p/\rho)\end{pmatrix} + \begin{pmatrix}0\\ p\partial\xi_\alpha/\partial x_\beta\\ 0\end{pmatrix}, \tag{1}$$

where for a generalized frame of reference $\xi_\alpha = \xi_\alpha(x_\beta)$ $(\beta = 1, 2, 3)$, $(\alpha = 1, 2, 3)$ the quantities u_β and U_α represent the Cartesian and the contravariant velocity components $U_\alpha = u_\beta\partial\xi_\alpha/\partial x_\beta$, respectively. The quantity $\partial\xi_\alpha/\partial x_\beta$ denotes the Jacobian transformation matrix. The numerical flux F_α^c on the cell face, e.g. $i \pm \frac{1}{2}$, j, k, reads

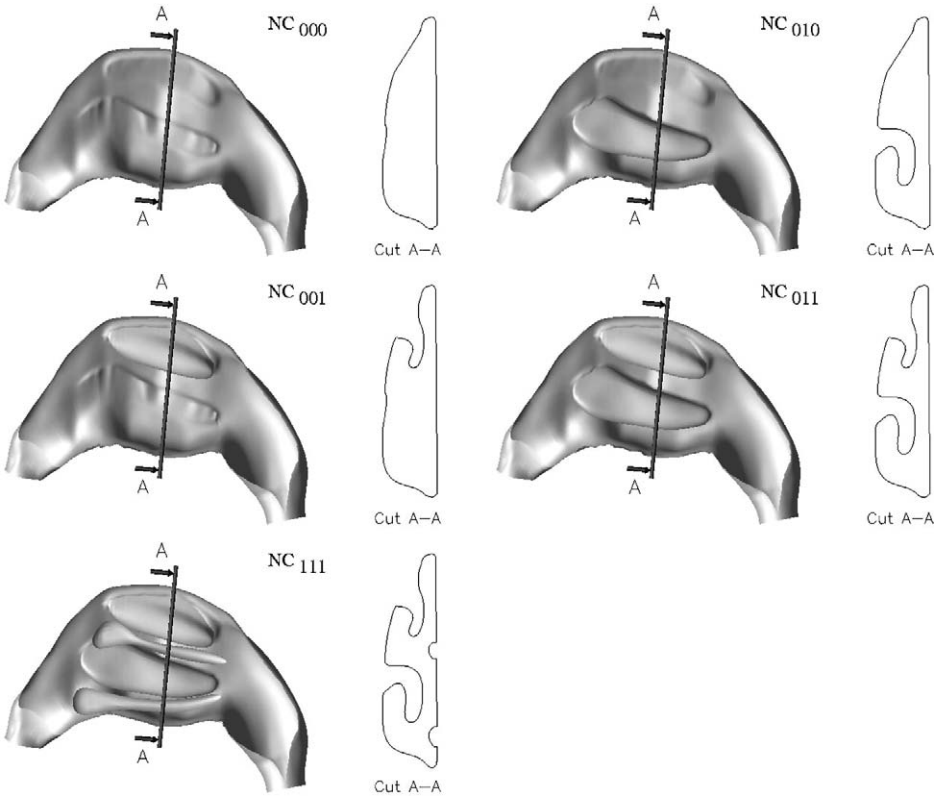

Fig. 2. Sketches of a coronal cross section to evidence the different nasal cavity geometries.

$$F_\alpha^c = \frac{1}{2}\left[\frac{Ma_\alpha^+ + Ma_\alpha^-}{2}\left(f_\alpha^{c+} + f_\alpha^{c-}\right) + \frac{Ma_\alpha^+ + Ma_\alpha^-}{2}\left(f_\alpha^{c+} - f_\alpha^{c-}\right)\right], \tag{2}$$

where the fluxes $f_\alpha^{c\pm}$ and the Mach numbers $Ma_\alpha^\pm$ are determined by left and right interpolated variables that are obtained using a MUSCL (Monotonic Upstream Centered Schemes for Conservation Laws) approach for the primitive variables [17]. The various pressure-splitting formulations [18] to compute the remaining pressure term can be written in a general form

$$p^\pm = p^\pm\left(\frac{1}{2} \pm \chi Ma_\alpha^\pm\right). \tag{3}$$

The parameter χ defines what kind of pressure splitting scheme is used. A value $\chi = \frac{1}{2}$ yields the originally proposed AUSM scheme, whereas $\chi = 0$ represents a central splitting. For the given flow problem we set $\chi = \frac{1}{40}$ to avoid spurious waves near the exit boundary [19]. For the viscous stresses a central discretization is chosen.

This numerical method has been successfully validated by comparing previous preliminary numerical nasal cavity flow solutions and experimental data [20].

2.3. Boundary conditions

Since the Strouhal number can be considered much smaller than one at normal inspiration and expiration a steady state simulation can be conjectured to represent most of the significant features of the flow field. Under this assumption it suffices to develop a set of steady state boundary conditions.

A no-slip isothermal wall condition with $T_{\text{wall}} = T_\infty$ is assumed and the pressure gradient normal to the wall is set equal to zero. At the inlet we use the one-dimensional energy equation for compressible, isentropic flow to determine the speed for an isentropic expansion from a stagnation state via the well-known Saint-Venant and Wanzel equation.

Introducing the stagnation state 0 as a reference state $p = \tilde{p}/\tilde{p}_0$, $w = \tilde{w}/\tilde{a}_0$, $\rho = \tilde{\rho}/\tilde{\rho}_0$ and using the ideal gas law, the Saint-Venant and Wanzel equation can be rewritten to calculate the static pressure at a given expansion velocity

$$p_{\text{new}} = \left[1 - \frac{\kappa - 1}{2} p_{\text{old}}^{-2/\kappa} (\rho w)^2\right]^{\kappa/(\kappa-1)}, \tag{4}$$

where $\kappa = 1.4$ denotes the ratio of specific heats c_p/c_v for air. This equation can be used at the inflow boundary to iteratively compute the static pressure p_{new} at a new time step from the given value of ρw and an initial pressure p_{old} from the previous time step. Note that ρw is an integral value for the inflow cross section, i.e., the actual velocity distribution for the new time step has to be determined by the volume flux, i.e., by assuming a fully developed flow. At the outflow boundary the static pressure level p_∞ is prescribed plus a non-reflecting boundary condition formulation based on a sponge layer [21].

3. Experimental method

The simulations are accompanied by experimental velocity measurements in a set of parallel planes using the method of Digital Particle-Image Velocimetry (DPIV). The application of this optical method requires a fully unobstructed view into the inner flow region, i.e., a completely transparent model of the nasal cavity and an appropriate fluid with the same optical refractive index as the material of the model. In our previous work we used a model made of epoxy-based cast resin and the fluid tetraline [13]. Due to the complex handling of tetraline and the relatively high refractive index of epoxy-based resin, we apply an alternative method in this study described by Hopkins et al. [22], i.e., we use a rapid-prototyping process to manufacture a nose model made of silicone.

Owing to the small size and complex geometry of the human nasal cavity 1.5-scaled models (Fig. 3) are built. The geometries are taken from the previously described CT-scans and stored as an STL data file. This is a common format for machining tools or rapid prototyping and it describes the 3-D surface as an unstructured grid. From this data a "negative" kernel of the nasal passage is generated with rapid prototyping. The material is a water soluble cornstarch, which is glued layer by layer in a 3-D printing device. The corresponding positive is obtained by casting the kernel in a transparent silicone block. After curing the kernel is washed out yielding a silicone block with the nasal passage as internal flow geometry.

As already described for the numerical simulations several geometry variations are investigated with special focus on the influence of the turbinates on the flow field. Therefore, in addition to the upper-and-lower-turbinates model without spurs NC_{011}, two other models are manufactured, the NC_{001} model with only the upper turbinate and the NC_{010} model with only the lower turbinate. Like in the numerical investigations the septum is assumed as a planar surface in all models but the NC_{111} case, which has two spurs on the inner side.

The models are placed within a flow loop with water/glycerol as carrier medium (Fig. 4). The complete model is fully immersed within a squared basin made of acrylic glass to which the inflow and outflow devices are connected. The inlet of the nostril region possesses the shape of a smooth nozzle being connected to the container box. The flow through the nasal cavity exits into the throat, which is simulated by a long straight pipe. The refractive index of the silicone matches that of a volume ratio mixture of glycerol to water of 55%. The mass flow rate is adapted to the

Fig. 3. The NC_{001} (left), NC_{011} (center), and NC_{010} (right) silicone models which still contain the cornstarch kernel.

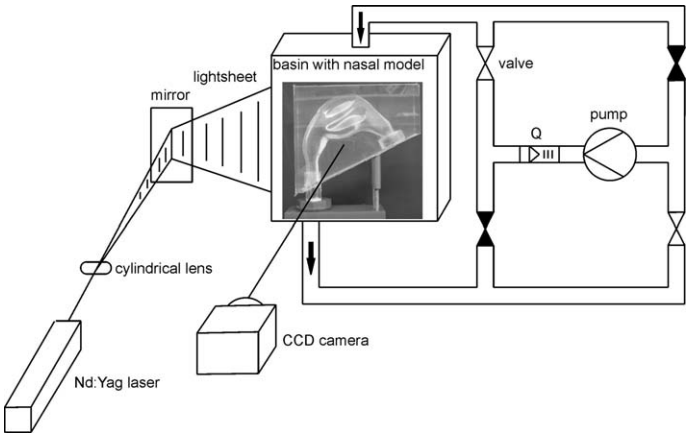

Fig. 4. Principal sketch of the DPIV setup and the optical arrangement for measurements in sagittal planes parallel to the septum.

characteristic air flow parameters in the nose by keeping the Reynolds number constant. Inspiration and expiration are produced by changing the flow direction in the pipe system.

The hydrogen bubble technique is used to produce fine air bubbles as tracer particles, which are recorded by the CCD camera to visualize and quantitatively measure the flow. For the DPIV measurements the fluid is illuminated in planar laser light sheets generated by a double pulse Nd:YAG laser. The light sheets are arranged in sagittal planes parallel to the septum and in coronal cross-sections of the nasal passage. The 20 sagittal planes are 1 mm apart and 10 coronal planes cover the flow between the nostril and the throat. All measurements are taken with a single DPIV camera. Since this study focuses on the investigation of the mean flow behavior, i.e., the mean velocity profiles and complex flow patterns such as vortex structures or separation areas, the results are based on an average of 50 DPIV recordings.

4. Results

At inspiration and expiration we assume volume fluxes for respiration at rest of 159.15 ml/sec and 127.32 ml/sec that result in Reynolds numbers of $Re = 500$ and $Re = 400$, respectively. Note that in this study the mean Reynolds number based on the mean channel width for the highest considered volume flux of 318.31 ml/sec is in the range of 1030 to 1400 for all configurations investigated, which is why the flow in the numerical analysis is conjectured laminar. The reference length for the Reynolds number is based on the hydraulic diameter of the throat. Furthermore, as aforementioned the flow can be considered steady since the Strouhal number is much smaller than one.

The discussion will start with a comparison of numerical and experimental results. We will focus on the NC_{011} geometry since the other geometry variants show a similar quality of agreement. The further investigation will be based solely on numerical results. Next, the influence of the Reynolds number on the flow field will be concisely discussed. Finally, the detailed analysis of the impact of geometric changes on the flow structure at inspiration and expiration will be presented. Distributions of the pressure on the surface and on predefined paths as well as skin friction and streamline patterns are used to evidence the features of the various flow problems.

In Figs. 6–11 numerical and experimental findings for the NC_{011} geometry, i.e., upper and lower turbinates but no spurs, are juxtaposed at inspiration and expiration. For comparison reasons all results are interpolated on equidistant orthogonal grids. The locations of the four selected sagittal and coronal cross sections are indicated in Fig. 5. The cross sections were chosen such that they are in areas, where highly susceptible flow features, e.g., jet–wall interactions, single and double vortices, occur to make the experimental and numerical comparison more reliable. In Fig. 6 cross section 1 shows the flow over the lower and upper turbinate at inspiration. Upstream of the upper turbinate a small vortex-like structure occurs, which is detected by the simulations and the experiments. The cross sections 2–4 in Fig. 6 present mainly the deflection of the flow by the lower and upper turbinate. A closer look reveals a good agreement as far as the angle and the magnitude of the velocity vectors are concerned. Fig. 7 contains the velocity distribution at expiration. The visualization in cross section 1, which shows the flow field between the septum and the turbinates, evidences the same overall flow orientation in the computed and the measured distributions. The cross sections 2–4

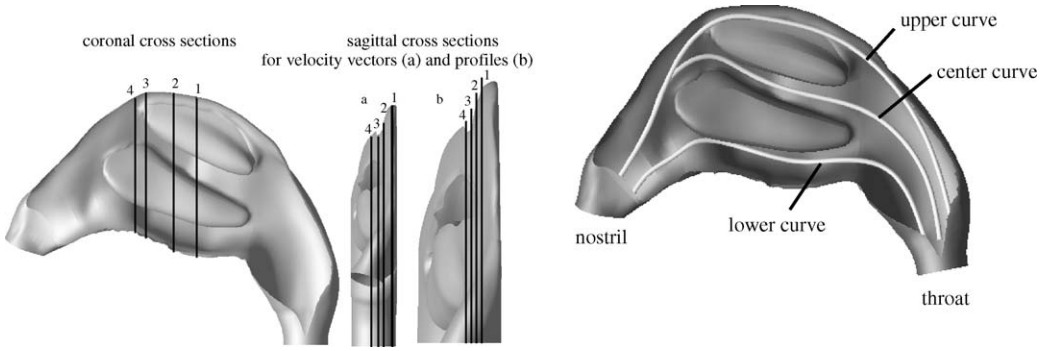

Fig. 5. Positions of coronal (left) and sagittal (center) cross sections, prescribed geometrical curves for pressure plots (right).

exhibit a jet-like flow downstream of the throat that interacts with the outer boundary of the nasal cavity upstream of the upper turbinate. The flow structure in the vicinity of the interaction area does coincide in the numerical and the experimental findings. The same statement holds when the flow in the channel between the upper and lower turbinate, below the lower turbinate, and in the area downstream of the lower turbinate and upstream of the nostril are considered. Therefore, it is fair to conclude, that a convincing experimental and numerical agreement is proven by the velocity distributions in the sagittal cross section in Figs. 6 and 7. Furthermore, the comparison of Figs. 6, 7 emphasizes the mixing character of the flow at inspiration and the jet-like character at expiration.

In Figs. 8 and 9 numerical and experimental velocity profiles are presented for inspiration and expiration. The overall qualitative and quantitative agreement is quite satisfactory. At inspiration (Fig. 8) there is a tendency to higher flow rates in the middle channel between the upper and lower turbinate, while at expiration the flow prefers the upper channel above the upper turbinate due to the jet-like flow structure, which is defined by the throat geometry. However, even in the lower channel a higher maximum velocity is observed at expiration. Furthermore, the shape of the velocity distributions of the experimental and numerical findings substantiate the assumption of a laminar flow, since the velocity profiles are by far not as fully developed as they are to be expected in turbulent pipe or channel type flow.

In Figs. 10, 11 the velocity distributions at inspiration and expiration in several coronal sections of the NC_{011} geometry are shown, where cross section 1 is closest to the throat and cross section 4 is nearest the nostril region (Fig. 5). In Fig. 10 there is a double vortex structure visible between the lower and upper turbinate in cross sections 1 and 2. The qualitative agreement between the computations and measurements is definitely good in the cross section near the throat. A slight discrepancy occurs in cross section 4 since the vortex structure above the lower turbinate is not observed before cross section 3 in the experiments whereas the numerical analysis reveals such a vortical structure already in cross section 4. When the less intricate flow region below the lower turbinate is considered, again a satisfactory correspondence between numerics and measurements is visualized. At expiration a strong flow from the region between the upper and lower turbinate through the area between the lower turbinate and the septum is evidenced in cross sections 1 and 2 in Fig. 11. Closer to the nostril, i.e., in cross sections 3 and 4, a converging flow structure with a separation line on the septum is determined in almost the same location in the numerical and experimental findings. In brief, the results in Figs. 6–11 show the good agreement of the computations and the measurements in the sagittal and coronal cross sections and prove the numerical method and the laminar flow assumption to yield the proper description of the overall flow structure.

In the following discussion of purely numerical results, the flow field of the NC_{111} geometry serves as a reference solution. The findings for the NC_{011} configuration will be presented to discuss the sensitivity of the flow to changes in Reynolds number. Since the spurs do not show any significant impact on the flow topology, i.e., the NC_{111} and the NC_{011} streamline patterns look more or less alike, the remaining of this paper will focus on comparing the flow fields of the NC_{111}, NC_{001}, NC_{010} and NC_{000} configurations.

It goes without saying that during the respiration cycle also higher Reynolds numbers occur than $Re = 400$ or $Re = 500$, respectively. To investigate the impact of volume flux, i.e., a larger Reynolds number, Figs. 12, 13 show a comparison for two sets of Reynolds numbers, i.e., $Re = 500$ and $Re = 1000$ at inspiration and $Re = 400$ and $Re = 790$ at expiration, the larger values of which belong to volume fluxes of 318.31 ml/sec and 251.46 ml/sec.

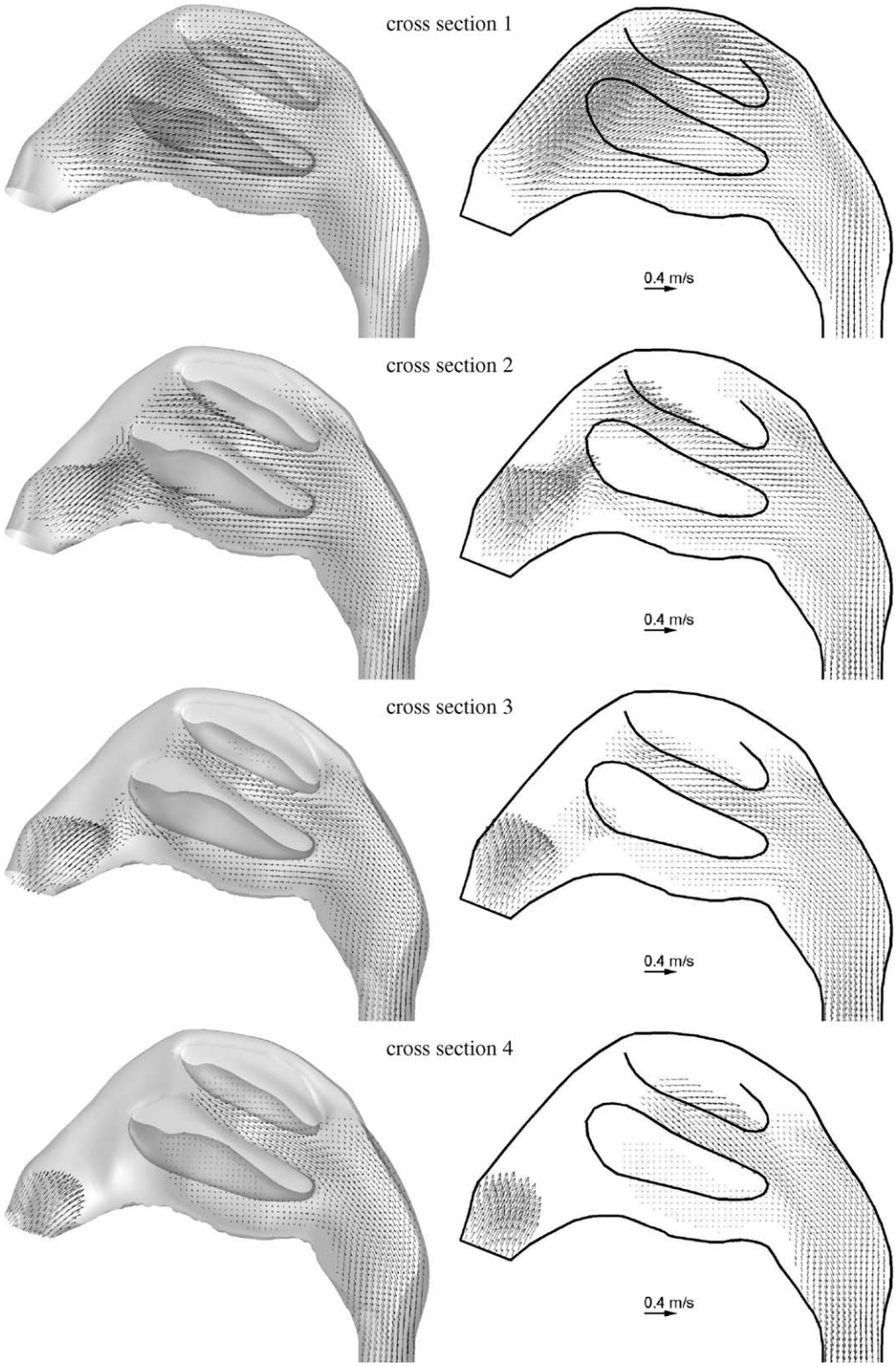

Fig. 6. Velocity field in several sagittal cross sections at inspiration ($Re = 500$); comparison of numerical (left) and experimental (right) results.

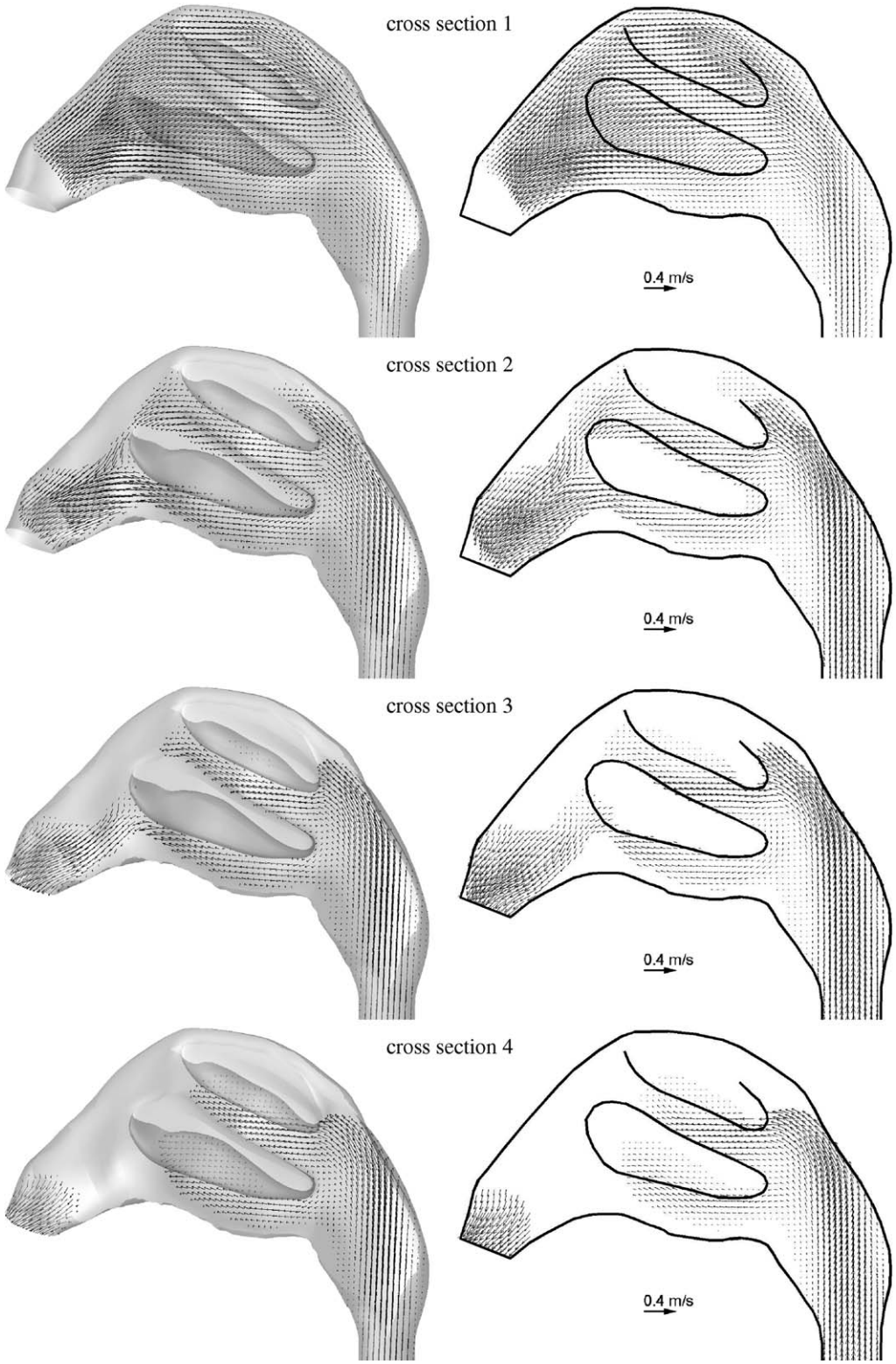

Fig. 7. Velocity field in several sagittal cross sections at expiration ($Re = 400$); comparison of numerical (left) and experimental (right) results.

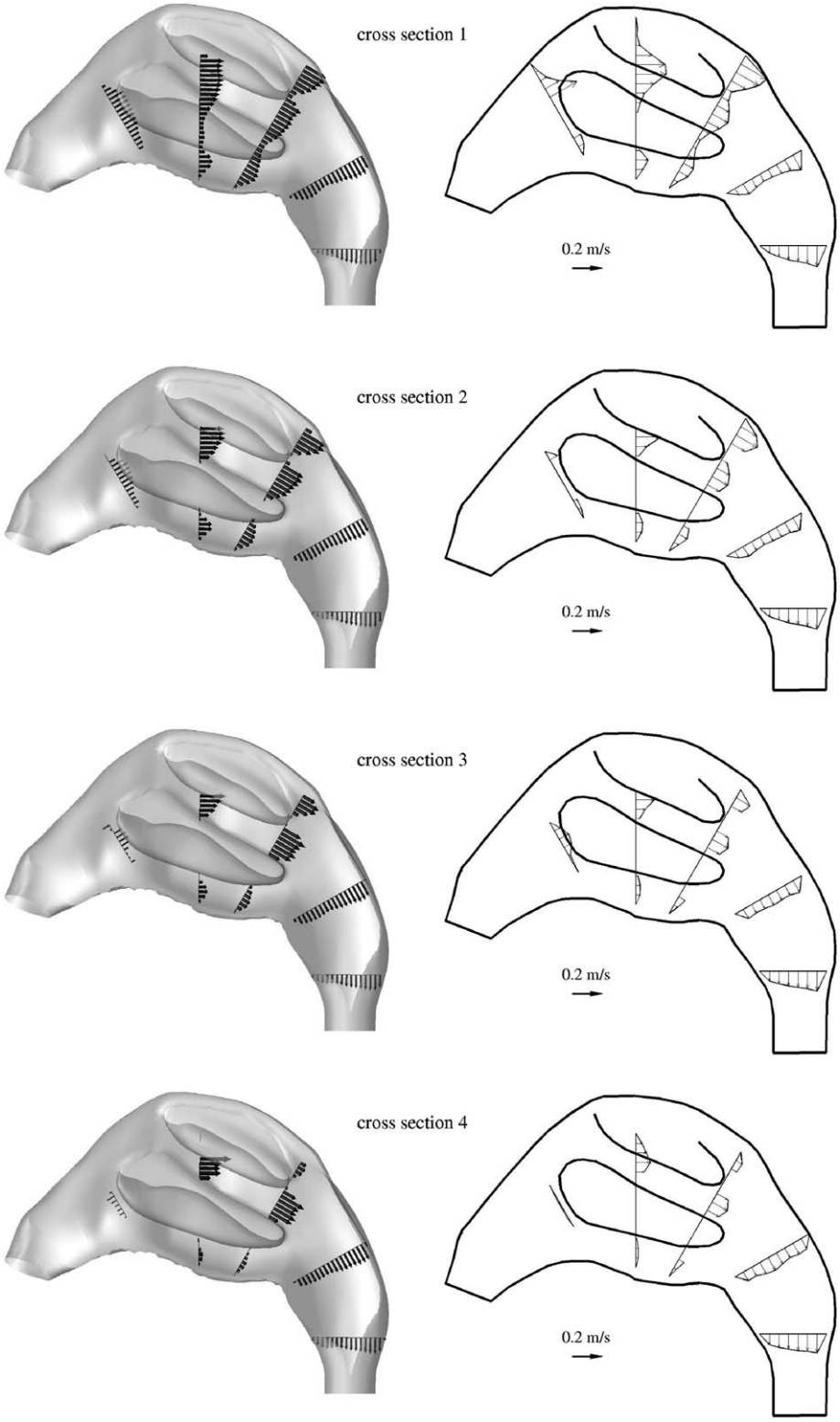

Fig. 8. Velocity profiles at various positions in several sagittal cross sections (top to bottom) at inspiration ($Re = 500$); comparison of numerical (left) and experimental (right) results.

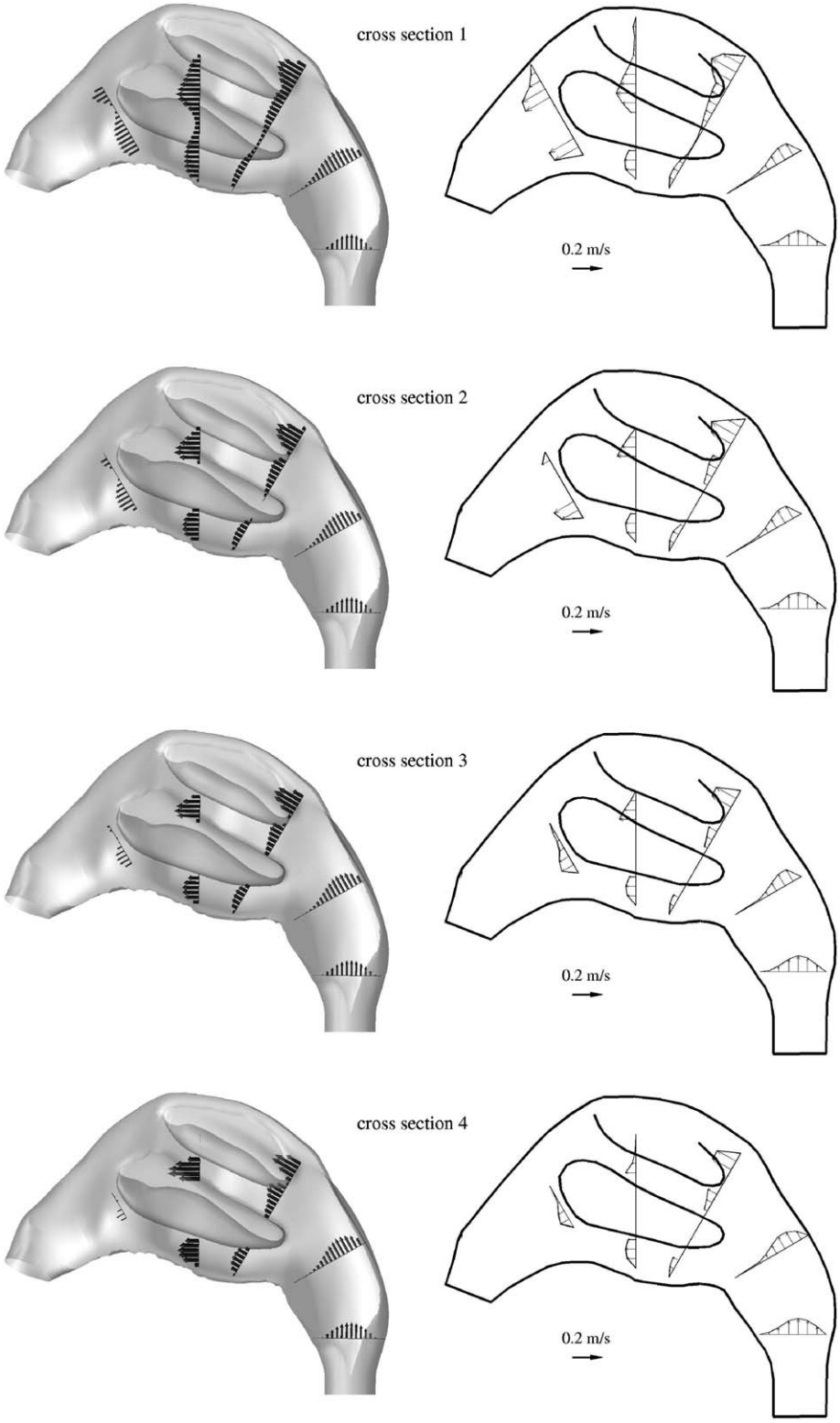

Fig. 9. Velocity profiles at various positions in several sagittal cross sections (top to bottom) at expiration ($Re = 400$); comparison of numerical (left) and experimental (right) results.

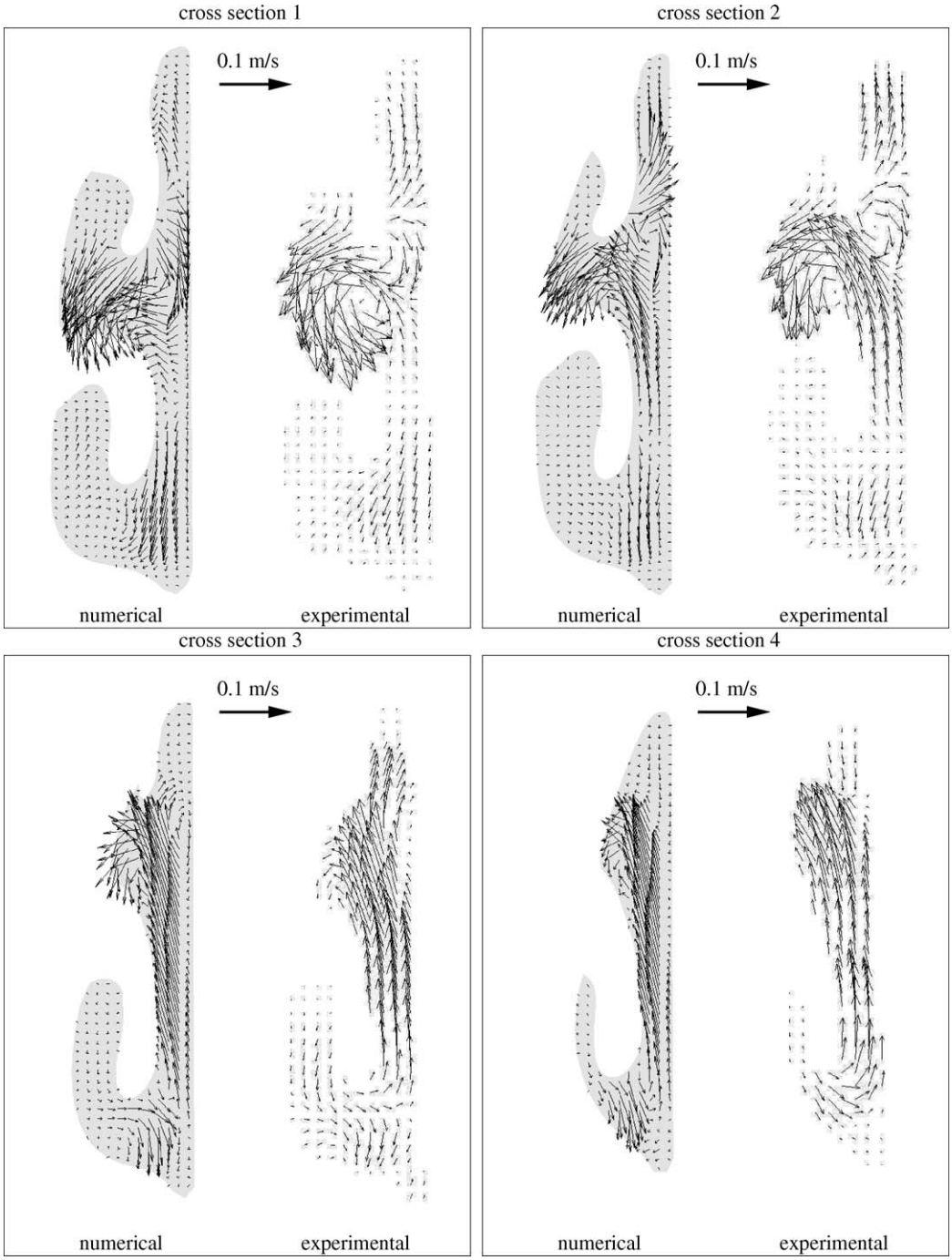

Fig. 10. Velocity field in several coronal cross sections at inspiration ($Re = 500$); comparison of numerical (left) and experimental (right) results.

Pressure distributions along three prescribed geometrical curves (Fig. 12), which are located in the lower, middle, and upper channel of the nasal cavity (Fig. 5), indicate that the expiration phase is hardly impacted by the Reynolds number. There is only a slight change in the nostril pressure level. This observation is substantiated by the streamline patterns in Fig. 13. At inspiration the Reynolds number increase results in more pronounced vortex structures, which is evidenced by the local pressure minima and maxima in Fig. 12 as well as by the streamline pattern upstream of the upper and lower turbinate in Fig. 13. The dependence of the overall flow structure on the Reynolds number in the

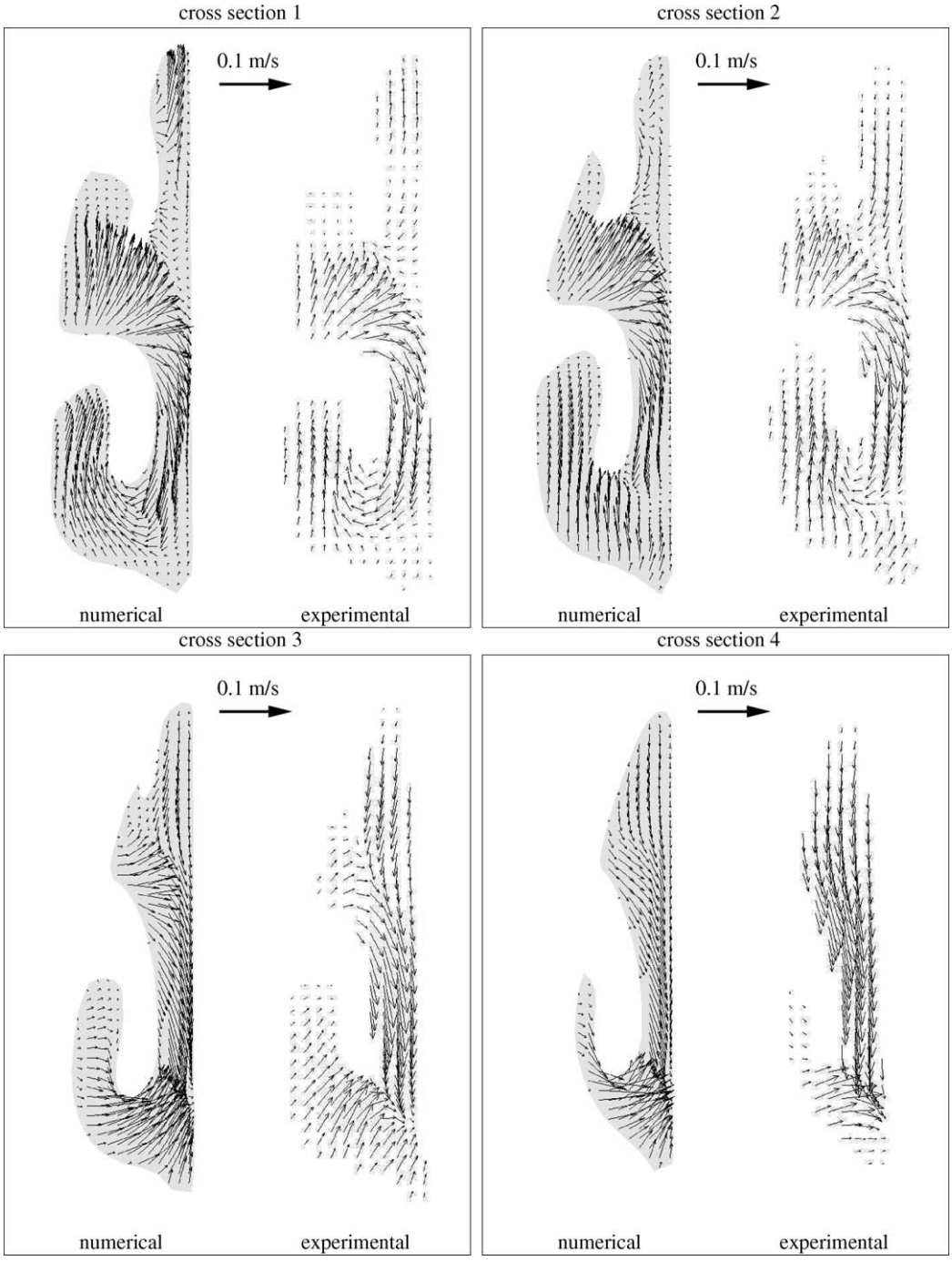

Fig. 11. Velocity field in several coronal cross sections at expiration ($Re = 400$); comparison of numerical (left) and experimental (right) results.

range of $400 \leqslant Re \leqslant 1000$, however, can be considered moderate since no additional flow features are observed. For this reason, the analysis of the impact of the geometry on the flow structure is based on $Re = 500$ and $Re = 400$. Note, this comparison was performed on 60,000 and 250,000 cell meshes and in neither case the flow structures in the high Reynolds number solutions were significantly different from the low Reynolds number findings.

Fig. 14 shows pressure contours on the surface of those four geometries at inspiration and expiration. It is evident that at inspiration the major changes in the pressure distribution occur almost independent from the configuration

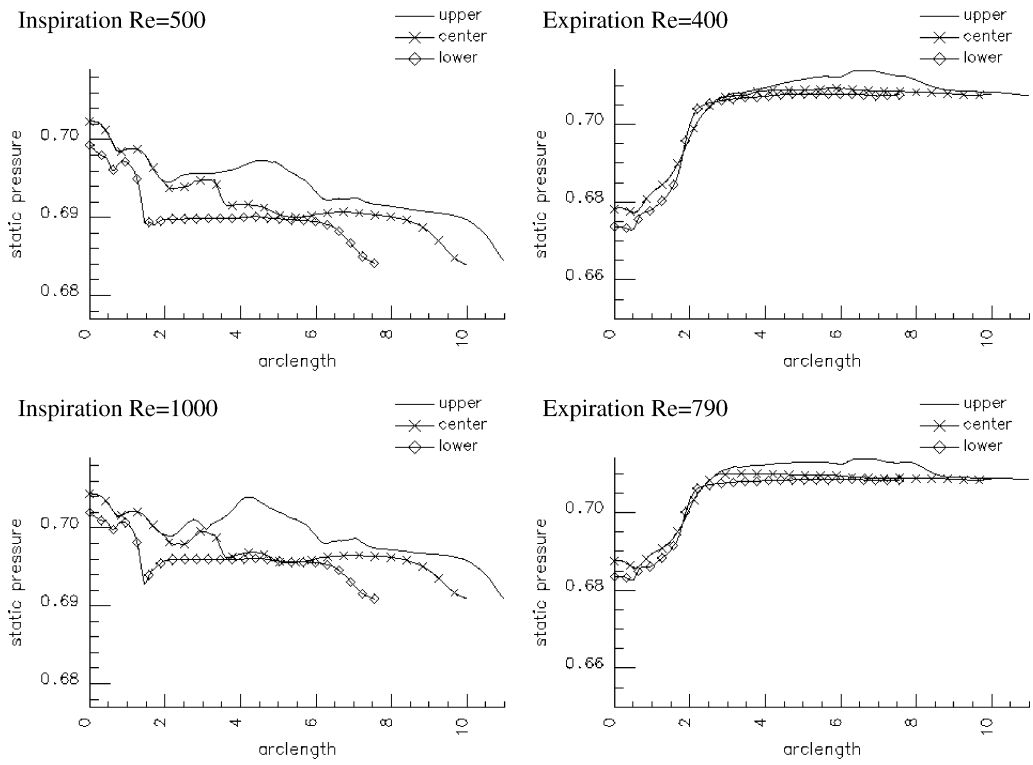

Fig. 12. Static pressure distribution on three prescribed geometrical curves for the NC_{011} configuration at different Reynolds numbers.

approximately two to three hydraulic diameters downstream of the nostril region. This pronounced gradient is not determined by the turbinates but by the sudden expansion region, since it is also observed in the no-turbinate NC_{000} case. It goes without saying that due to the larger blockage the pressure drop is stronger in the NC_{111} problem. In the region of the turbinates and spurs and in the throat area the pressure alters only slightly. However, a closer look for the NC_{001} geometry indicates that a slight pressure gradient is generated above the upper turbinate.

A similar behavior is determined for the expiration flow field (Fig. 14, right). That is, the most dramatic changes in the pressure distribution are generated by the sudden convergence of the channel in the vicinity of the nostril and the pressure distribution on the NC_{001} geometry, which lacks the lower turbinate, differs more from the reference case NC_{111} than that without the upper turbinate NC_{010}. Furthermore, when primarily the lower region of the nasal cavity is considered, the pressure distribution of the NC_{001} case is hardly any different from that of the geometry without any turbinate. These results emphasize the major role of the sudden expansion region and the lower turbinate at inspiration and expiration.

This observation is quantitatively evidenced by the pressure distributions in Fig. 15 along three prescribed geometrical curves (Fig. 5). For each configuration the major pressure variation occurs in the same area. However, at expiration the pressure distributions for the different curves within the nasal cavity are fairly smooth and do almost coincide, whereas at inspiration the distributions possess a less monotone behavior and a clear discrepancy between the upper and the remaining paths is computed. That is, in the former case there is only a slight impact of the geometry on these distinct pressure curves, which can be interpreted as a first indication of less influence of the nasal configuration on the overall flow behavior at expiration. Only when air is inhaled the turbinates and the spurs, i.e., the NC_{111} geometry is considered, ensure a somewhat stronger acceleration near the entrance of the lower channel and cause a plateau-like pressure behavior on a lower pressure level than for the other configurations (Fig. 15). Furthermore, note the pronounced peak in the pressure distribution along the upper path when the lower turbinate is removed, i.e., in the NC_{001} and NC_{000} configurations in Fig. 15, compared to the distribution of the reference geometry NC_{111}. Although these deviations occur at inspiration and expiration it is the distribution for the NC_{000} configuration in Fig. 15 that emphasizes the stronger susceptibility of the flow field on the nose geometry at inspiration than at expiration.

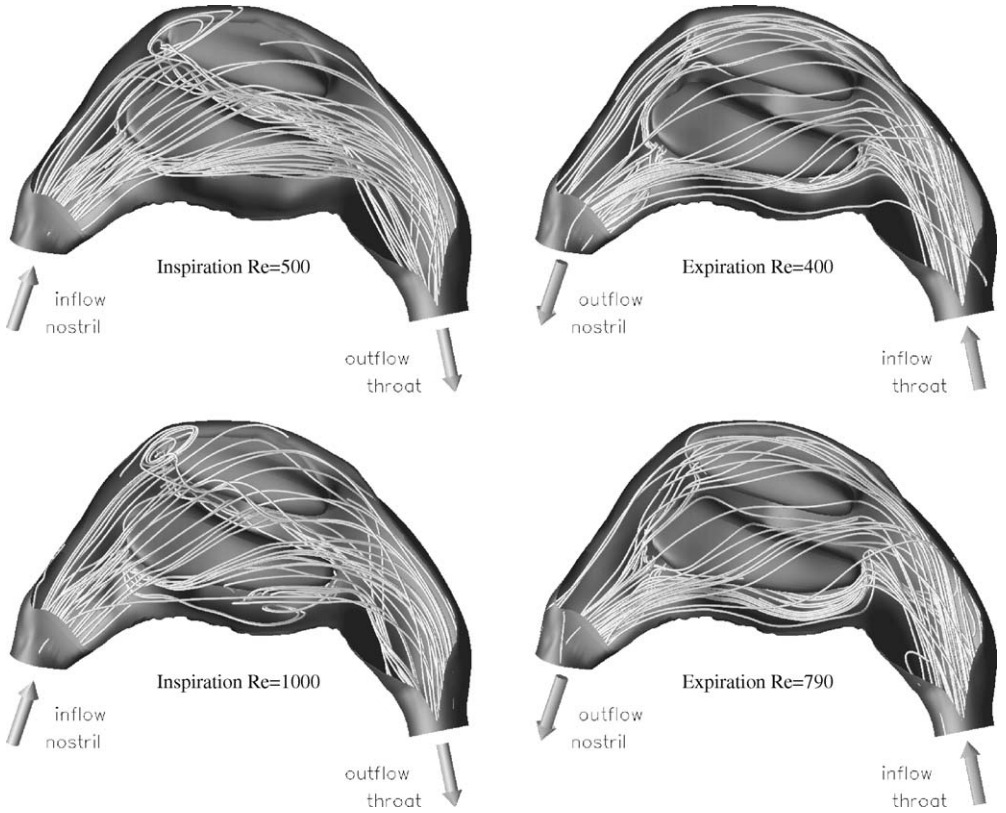

Fig. 13. Streamlines for the NC_{011} configuration at different Reynolds numbers.

The smallest cross section downstream of the nostril can be approximately identified as the first pronounced decrease in the pressure distribution for the lower geometrical curve at inspiration in Fig. 15. This pressure drop is weakened from the NC_{111} case to the NC_{000} case due to the removal of the turbinates and spurs. A second sharp pressure decrease is evident for the center curve before it enters the center channel (Fig. 15, NC_{111} case). This is related to the converging channel between the upper and lower turbinates. This pressure gradient almost vanishes when the upper turbinate is removed (Fig. 15, NC_{010} case).

Fig. 16 shows the wall shear stress distribution at inspiration and expiration. As already indicated by the pressure contours on the surface, high shear stresses occur in the nostril region for both respiration states and all nose configurations. Furthermore, also independent from the configuration considered, the larger wall shear stresses are observed in the lower part of the sudden expansion area located below the upstream tip of the lower turbinate. In other words, in the sudden expansion area the flow in the immediate vicinity of the wall does not possess any strong susceptibility to the nose geometry defined by the spurs and the turbinates. This changes when the distribution further downstream is considered. Due to the missing septum spurs steeper gradients occur in the wall shear stress distribution on the lower turbinate in the NC_{010} case than in the NC_{111} case. A similar behavior is observed when the wall shear stress distributions on the upper turbinate of the NC_{111} and NC_{001} configurations are juxtaposed. That is, the spurs smooth the streamwise distribution of the velocity gradients on the turbinates.

The streamlines in Fig. 17 evidence the vortices and recirculation regions in the flow field near the nostril and the throat. At inspiration a horseshoe-like vortex is visible upstream of the lower turbinate for the NC_{111} and NC_{010} configurations. By juxtaposing the streamline patterns of the NC_{111}, NC_{010} and NC_{001}, NC_{000} configurations in Fig. 17 it appears that especially the lower turbinate and the spurs seem to serve as guide vanes to ensure, e.g., a homogeneous velocity distribution in the upper, center, and lower channels. That is, without the lower turbinate and the spurs the flow field is characterized by massive vortices, which impact the flow distribution in the nasal cavity and change the time it takes a fluid particle to move from the nostril to the throat. At expiration clearly less vortical structures up- and

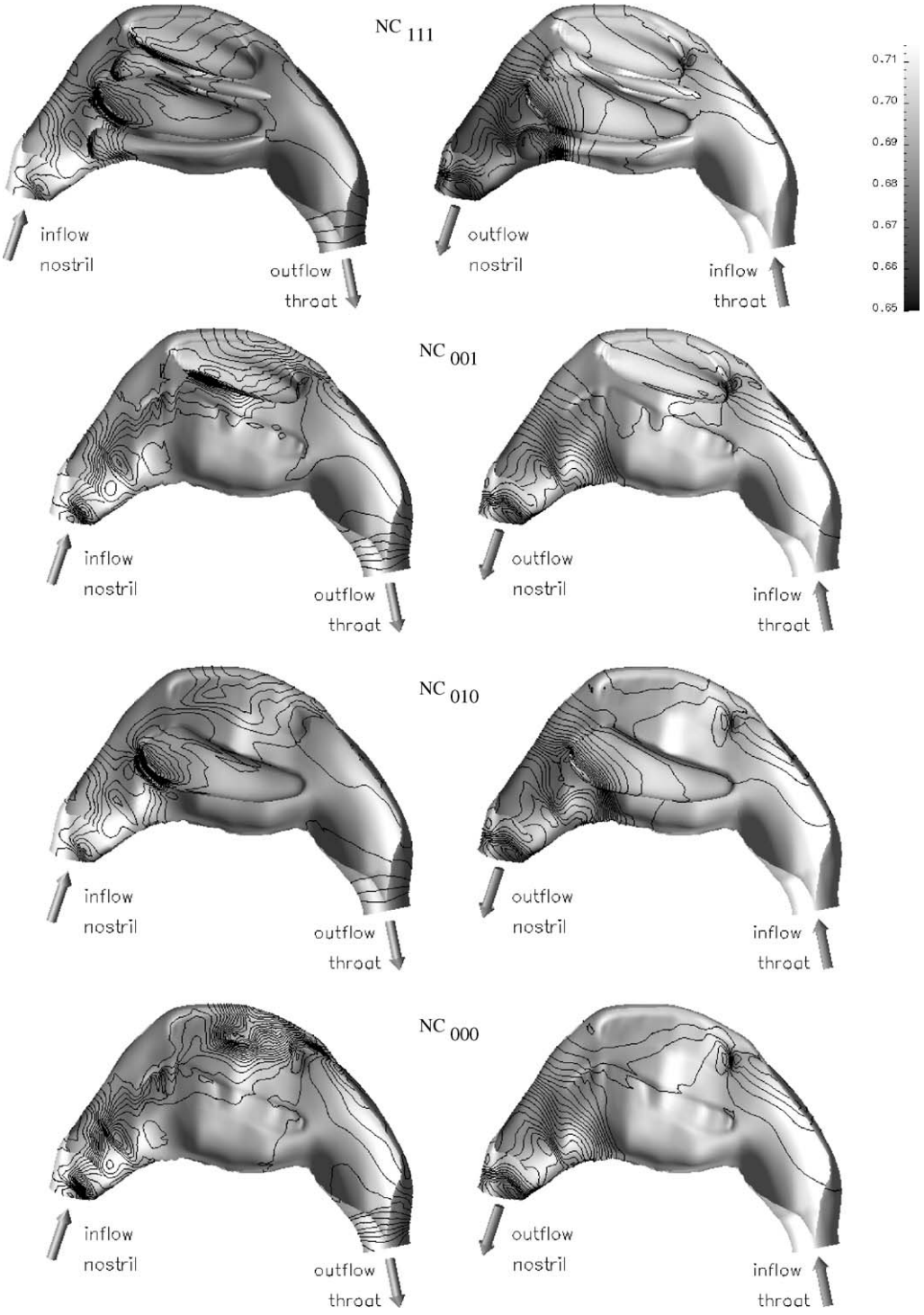

Fig. 14. Surface pressure contours at inspiration ($Re = 500$, left) and expiration ($Re = 400$, right) for the NC_{111}, NC_{001}, NC_{010}, and NC_{000} configurations (top to bottom).

downstream of the turbinates and spurs are detected emphasizing the smaller impact of the geometry on the flow field when air is exhaled.

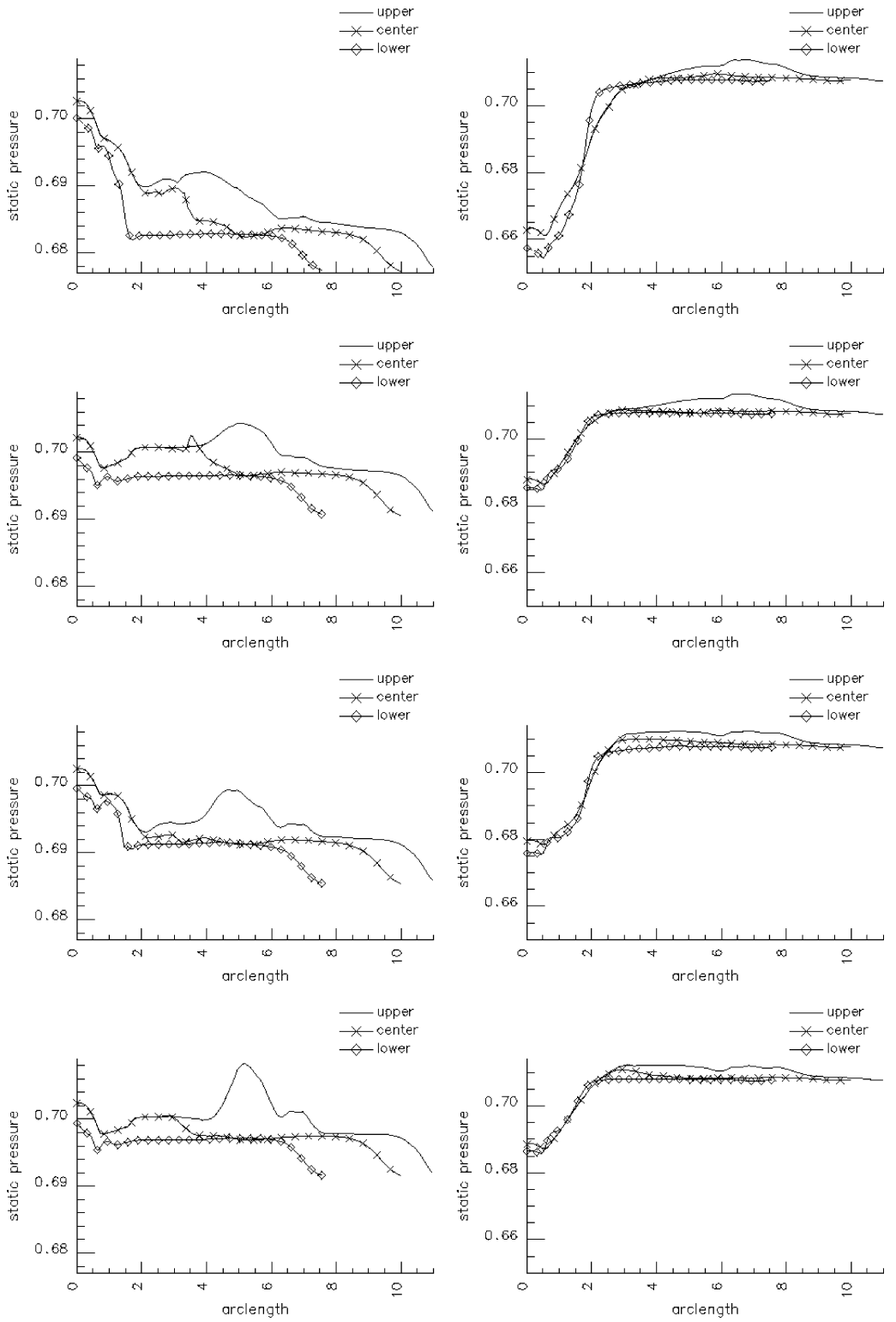

Fig. 15. Static pressure distribution on three prescribed geometrical curves at inspiration ($Re = 500$, left) and expiration ($Re = 400$, right) for the NC_{111}, NC_{001}, NC_{010}, and NC_{000} configurations (top to bottom).

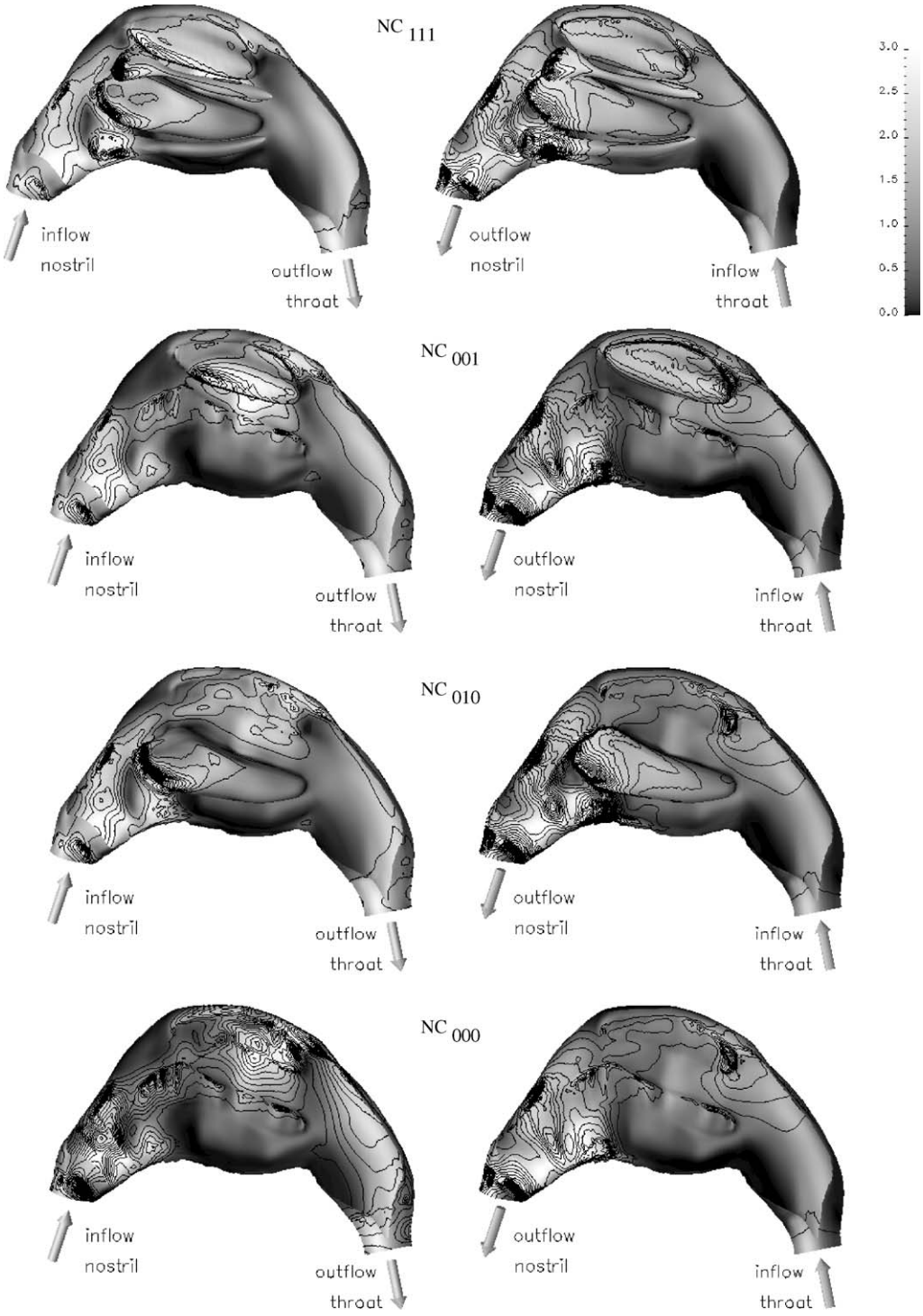

Fig. 16. Skin friction distribution at inspiration ($Re = 500$, left) and expiration ($Re = 400$, right) for the NC_{111}, NC_{001}, NC_{010}, and NC_{000} configurations (top to bottom).

Thus, it can be concluded that the reference geometry with turbinates and spurs appears to be optimized especially for inspiration to generate sufficient swirl to support mixing, which in conjunction with their surface area yields the correct tempering and moistening of the incoming air.

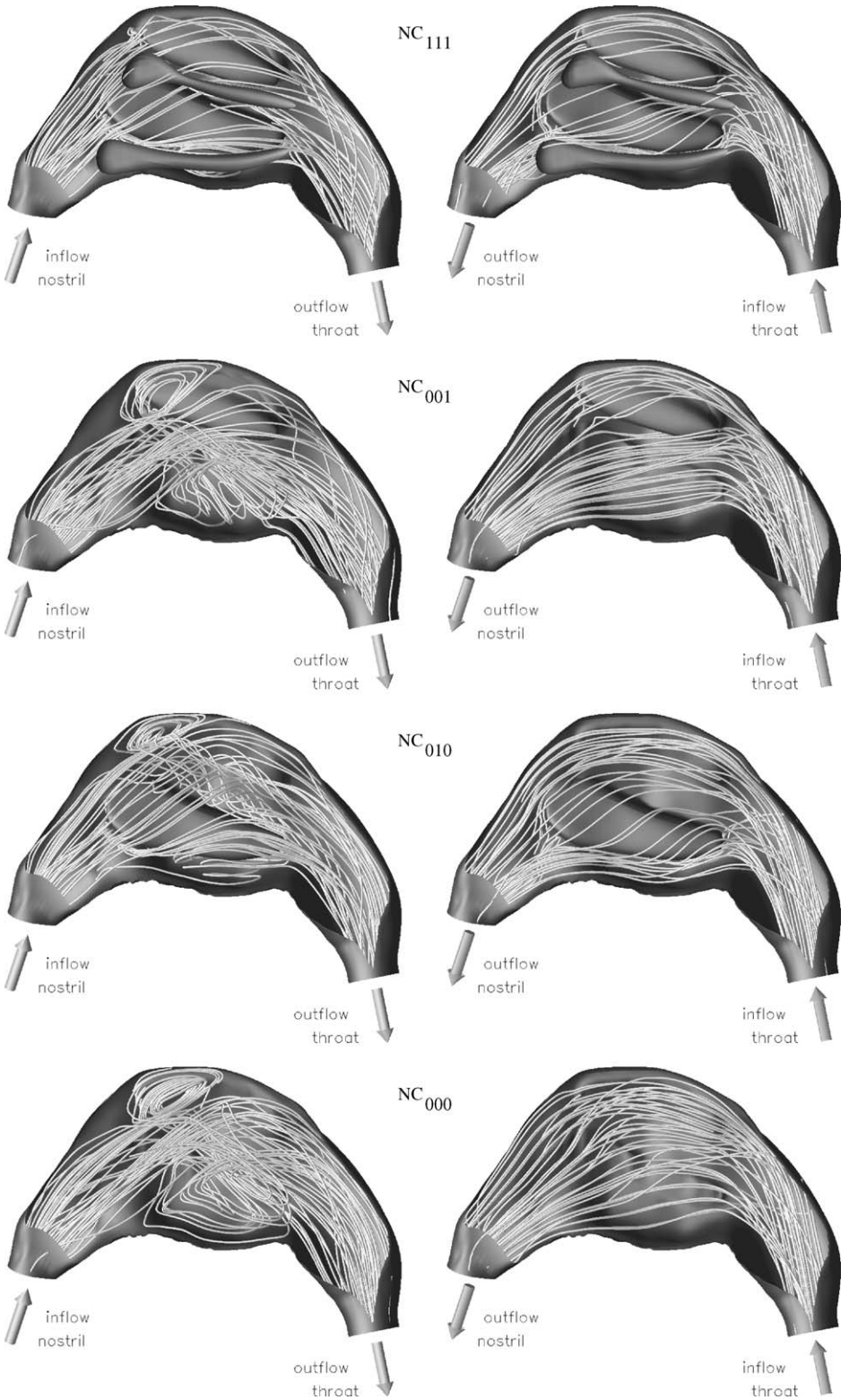

Fig. 17. Streamlines at inspiration ($Re = 500$, left) and expiration ($Re = 400$, right) for the NC_{111}, NC_{001}, NC_{010}, and NC_{000} configurations (top to bottom).

5. Conclusions

The comparison of the computations and the DPIV measurements for the nasal cavity flow showed a convincing agreement at inspiration and at expiration as far as the flow topology in several sagittal and coronal cross sections is concerned. Thus, it could be concluded that the laminar flow assumption is valid to capture the overall flow structure of the nose flow at Reynolds numbers ranging from 400 at expiration to 500 at inspiration.

Using this result the numerical method was applied to compute the flow field of several nasal cavity configurations at inspiration and expiration to analyze the susceptibility of the flow to the geometry. The investigation shows that the inspiration phase is much more sensitive to any kind of geometry change than the expiration period. The turbinates serve as guide vanes to ensure a homogeneous velocity distribution in the lower, center, and upper channel between the nostril and the throat. The lower turbinate possesses the major impact on the velocity field and the pressure distribution since this is the part of the nose geometry that primarily interacts with the flow in the sudden expansion region.

Acknowledgement

This research has been conducted under research grant WE 2186/5. The financial support by the German Research Foundation (DFG) is gratefully acknowledged.

References

[1] G. Schlöndorff, Computer assisted surgery: historical remarks, Computer Aided Surgery 3 (1998) 150–152.
[2] M. Wolf, S. Naftali, R. Schroter, D. Elad, Air-conditioning characteristics of the human nose, J. Laryngology Otology 118 (2004) 87–92.
[3] K. Keyhani, P.W. Scherer, M.M. Mozell, A numerical model of nasal odorant transport for the analysis of human olfaction, J. Theor. Biol. 186 (1997) 279–301.
[4] D. Pless, T. Keck, K. Wiesmiller, G. Rettinger, A.J. Aschoff, T.R. Fleiter, J. Lindemann, Numerical simulation of air temperature and airflow patterns in the human nose during expiration, Clin. Otolaryngol. 29 (2004) 642–647.
[5] D. Elad, R. Liebenthal, B.L. Wenig, S. Einav, Analysis of air flow patterns in the human nose, Med. & Biol. Eng. & Comput. 31 (1993) 585–592.
[6] I. Hahn, P.W. Scherer, M.M. Mozell, Velocity profiles measured for airflow through a large-scale model of the human nasal cavity, J. Appl. Physiol. 75 (1993) 2273–2287.
[7] J.T. Kelly, A.K. Prasad, A.S. Wexler, Detailed flow patterns in the nasal cavity, J. Appl. Physiol. 89 (2000) 323–337.
[8] S. Naftali, R.C. Schroter, R.J. Shiner, D. Elad, Transport phenomena in the human nasal cavity: a computational model, Ann. Biomed. Engrg. 26 (1998) 831–839.
[9] S.K. Kim, S.K. Chung, An investigation on airflow in disordered nasal cavity and its corrected models by tomographic PIV, Meas. Sci. Technol. 15 (2004) 1090–1096.
[10] G. Mlynski, S. Grützenmacher, B. Mlynski, B. Koch, Modelluntersuchungen zur Nasenmuschelchirurgie, Laryngo-Rhino-Otol. 72 (1993) 614–617.
[11] U. Bockholt, G. Mlynski, W.K. Müller, G. Voss, Rhinosurgical therapy planing via endonasal airflow simulation, Computer Aided Surgery 5 (2000) 175–197.
[12] H. Masing, Experimentelle Untersuchungen über die Strömung im Nasenmodell, Archiv klin. exp. Ohren-, Nasen- u. Kehlkopf-Heilk. 189 (1967) 59–70.
[13] Ch. Brücker, K.I. Park, Experimental study of velocity fields in a model of human nasal cavity by DPIV, in: S. Banerjee, K. Eaton (Eds.), Proc. 1st Int. Symp. "Turbulence and Shear Flow Phenomena", September 12–15, Santa Barbara, CA, 1999, pp. 831–836.
[14] GridPro, The CFD Link to Design, The Graphic Manager Manual, Programm Development Corp., 300 Hamilton Ave. Suite 409, White Plains, NY 10601, USA.
[15] E. Fares, M. Meinke, W. Schröder, Numerical simulation of the interaction of wingtip vortices and engine jets in the near field, AIAA Paper 2000-2046, June, 2000.
[16] M.S. Liou, Ch.J. Steffen Jr., A new flux splitting scheme, J. Comp. Phys. 107 (1993) 23–39.
[17] B. van Leer, Towards the ultimate conservative difference scheme V. A second-order sequel to Godunov's method, J. Comp. Phys. 32 (1979) 101–136.
[18] H. Choi, P. Moin, Effects of the computational time step on numerical solutions of turbulent flow, J. Comp. Phys. 113 (1994) 1–4.
[19] F. Rütten, W. Schröder, M. Meinke, Large-eddy simulation of low frequency oscillations of the Dean vortices in turbulent pipe bend flows, Phys. Fluids 17 (2005) 035107.
[20] I. Hörschler, M. Meinke, W. Schröder, Numerical simulation of the flow field in a model of the nasal cavity, Computers & Fluids 32 (2003) 39–45.
[21] T. Colonius, Numerically nonreflecting boundary and interface conditions for compressible flow and aeroacoustic computations, AIAA J. 35/7 (1997) 1126–1133.
[22] L.M. Hopkins, J.T. Kelly, A.S. Wexler, A.K. Prasad, Particle Image Velocimetry measurements in complex geometries, Exp. Fluids 29 (2000) 91–95.